Supplement of Atmos. Chem. Phys., 23, 13061–13085, 2023
https://doi.org/10.5194/acp-23-13061-2023-supplement

Atmospheric Chemistry and Physics
Open Access
EGU

Supplement of

Historical (1960–2014) lightning and LNO_x trends and their controlling factors in a chemistry–climate model

Yanfeng He and Kengo Sudo

Correspondence to: Yanfeng He (hyf412694462@gmail.com)

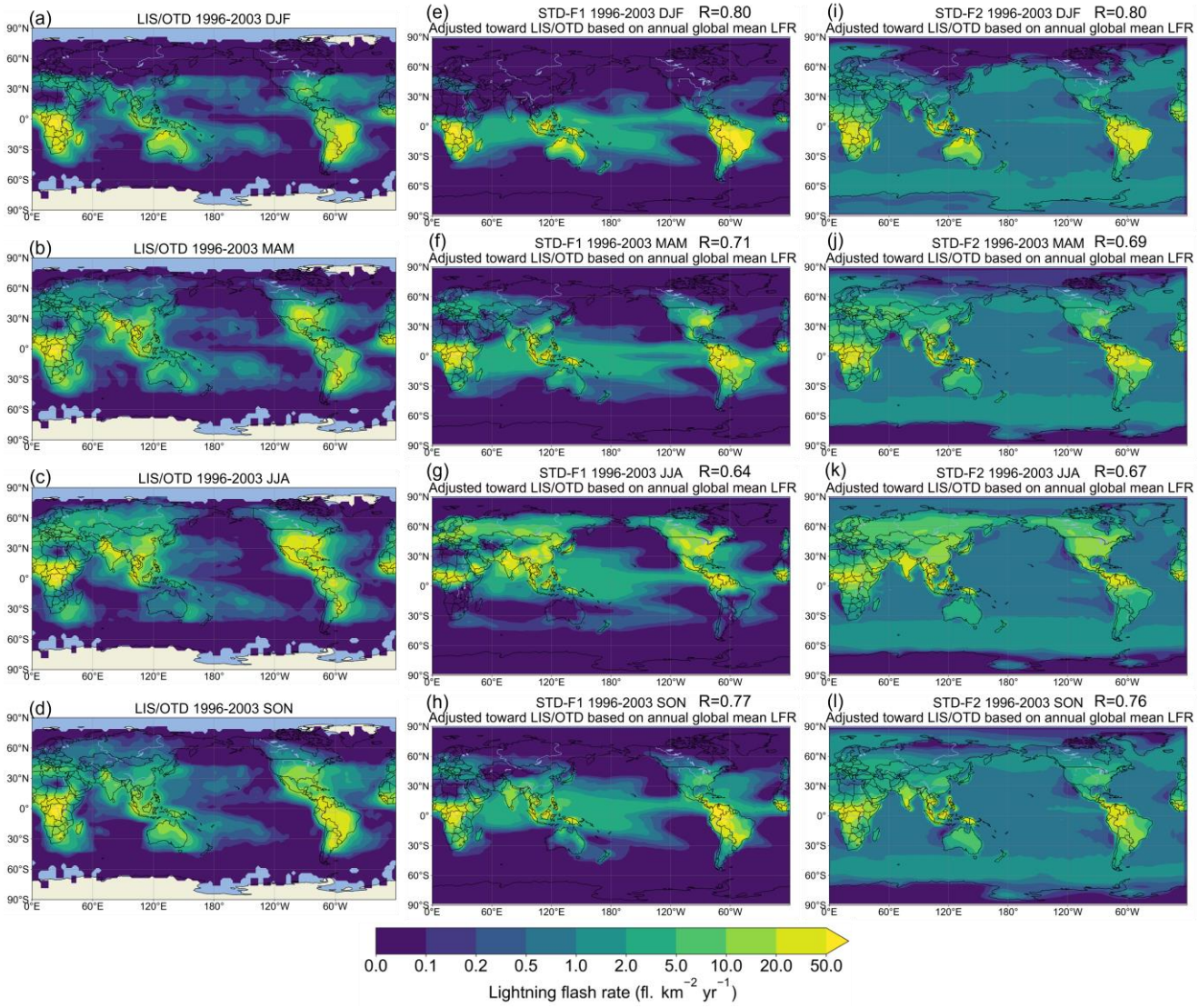

Figure S1: Global distributions of lightning flash rates (LFRs) during different seasons (1996–2003) from (a–d) LIS/OTD lightning observations, (e–h) the STD experiment with the ECMWF-McCAUL scheme used, (i–l) the STD experiment with the CTH scheme used. The LFRs shown in panels (e)–(l) were adjusted towards the LIS/OTD observations using a spatially uniform adjustment factor based on the annual global mean LFR of LIS/OTD observations and simulations. The spatial correlation coefficients (*R*) are shown in the titles of panels (e)–(l). The *R* values were calculated between LIS/OTD observations and simulations in the same season.

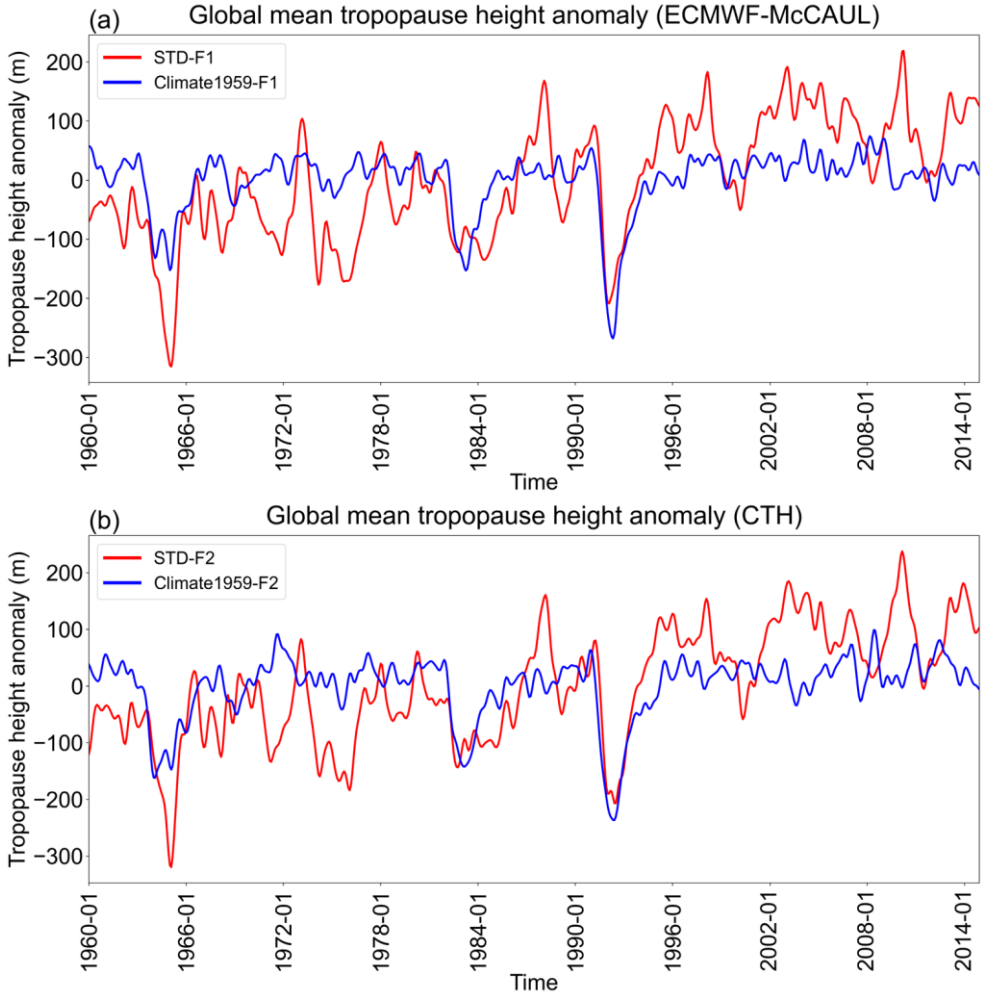

Figure S2: Monthly time-series data of global mean tropopause height anomaly with a 1-D Gaussian (Denoising) filter applied simulated using the ECMWF-McCAUL scheme (a) and the CTH scheme (b).

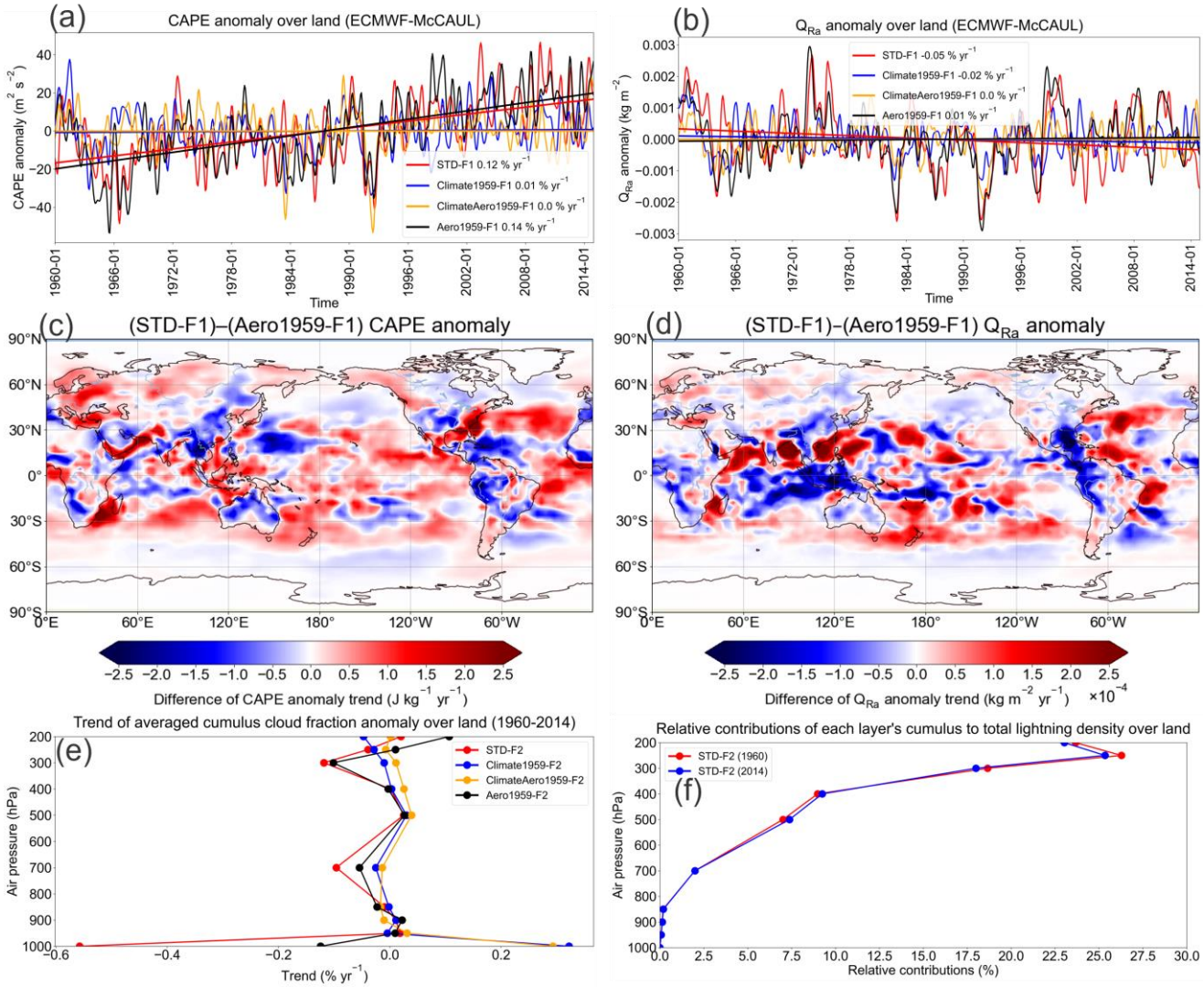

Figure S3: Figure S3, panels (a) and (b) respectively show monthly time-series data of terrestrial average CAPE and Q_{Ra} anomalies with a 1-D Gaussian (Denoising) filter applied and their fitting curves simulated using the ECMWF-McCAUL scheme. Figure S3, panels (c) and (d) respectively show differences in the CAPE anomaly trend ($\mathrm{J\,kg^{-1}\,yr^{-1}}$) and Q_{Ra} anomaly trend ($\mathrm{kg\,m^{-2}\,yr^{-1}}$) of the STD-F1 and Aero1959-F1 experiments in the global map. Figure S3e presents vertical profiles of the trend of the terrestrial average cumulus cloud fraction anomaly simulated by the CTH scheme. Figure S3f shows the relative contributions of each layer's cumulus to total lightning density over land regions in 1960 and 2014, as calculated from the outputs of the STD-F2 experiment.

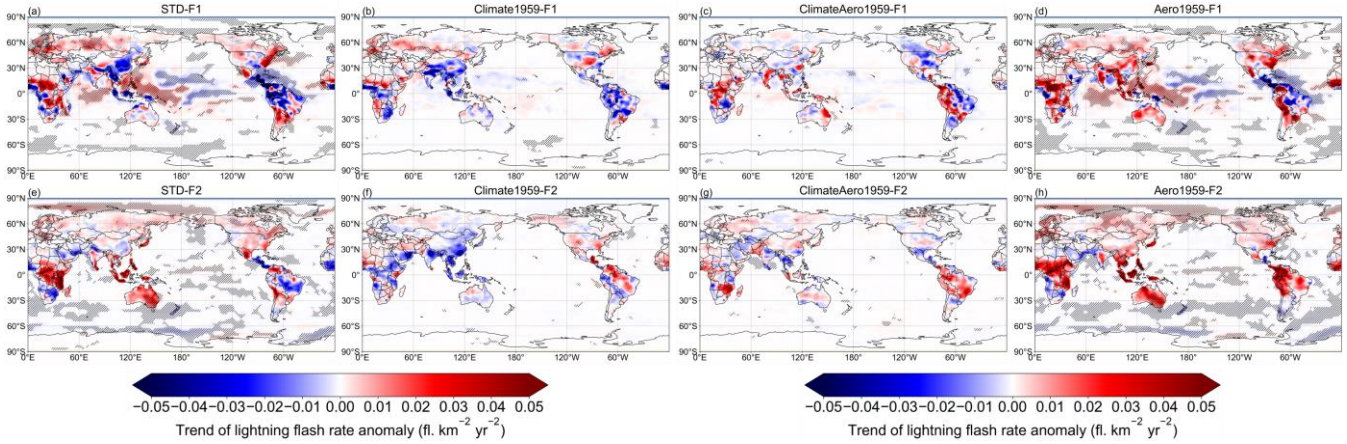

Figure S4: Trends of LFR anomalies in absolute value (fl. km^{-2} yr^{-2}) during 1960–2014 on the two-dimensional map. The trend at every point was calculated from the function of approximating curve for the 1960–2014 time-series data (LFR anomaly) at each grid cell. The area for which the trend was found to be significant using the Mann–Kendall rank statistic test (significance level inferred for 5%) is marked with hatched lines.

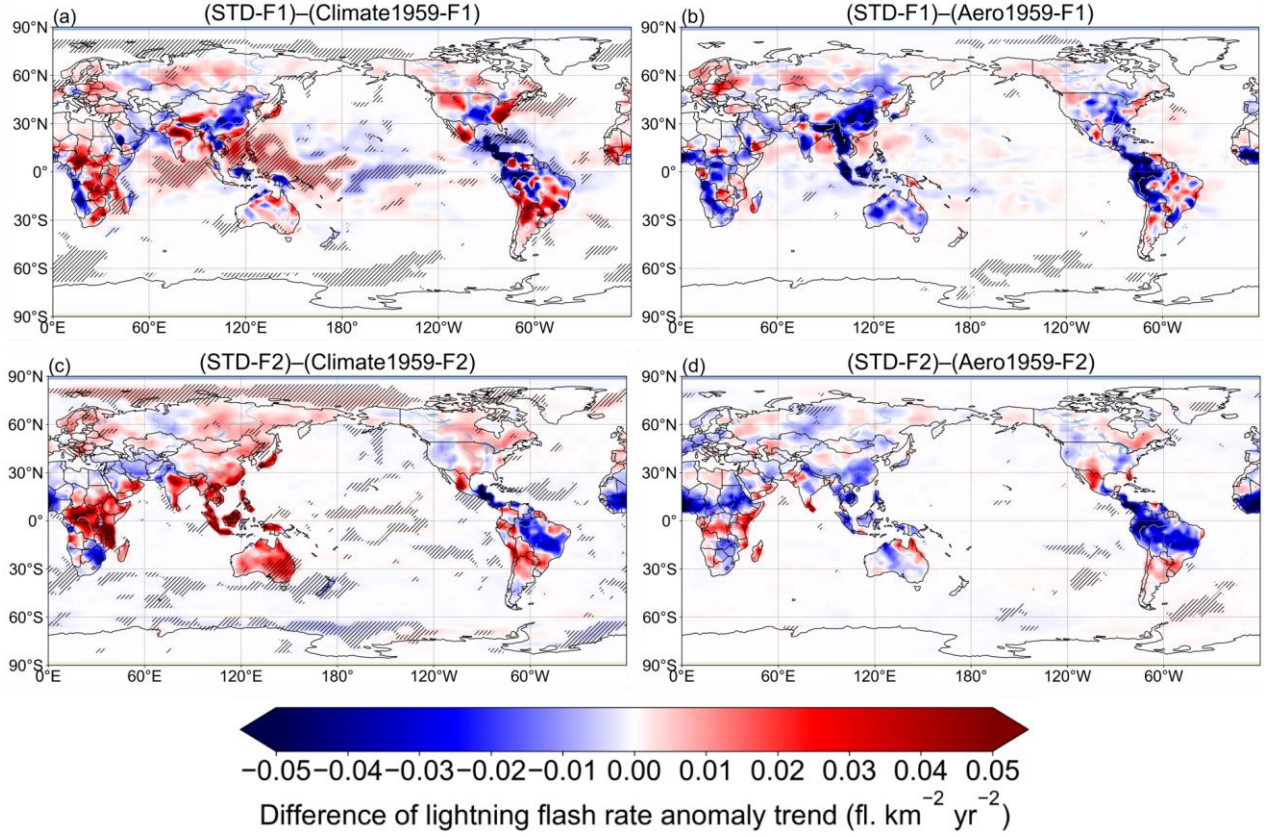

Figure S5: Differences in trends of LFR anomaly (fl. km^{-2} yr^{-2}) during 1960–2014 on the global map. The area for which the trend of the differences of LFR anomaly time-series data was found to be significant using the Mann–Kendall rank statistic test (significance level inferred for 5%) is displayed with hatched lines.

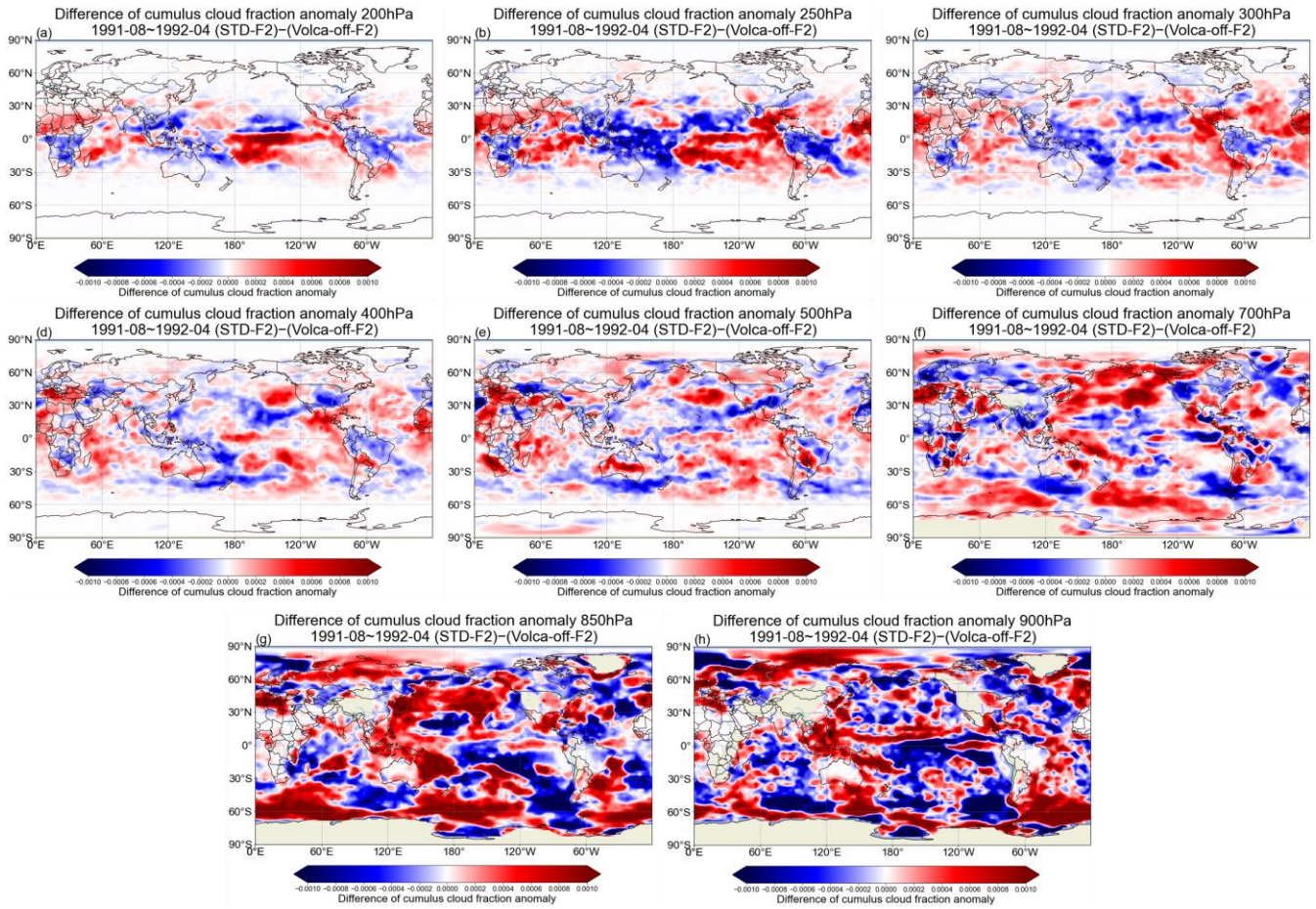

Figure S6: Differences of cumulus cloud fraction anomaly during 1991-08 – 1992-04 at different pressure levels between STD-F2 and Volca-off-F2 experiments on the global map.

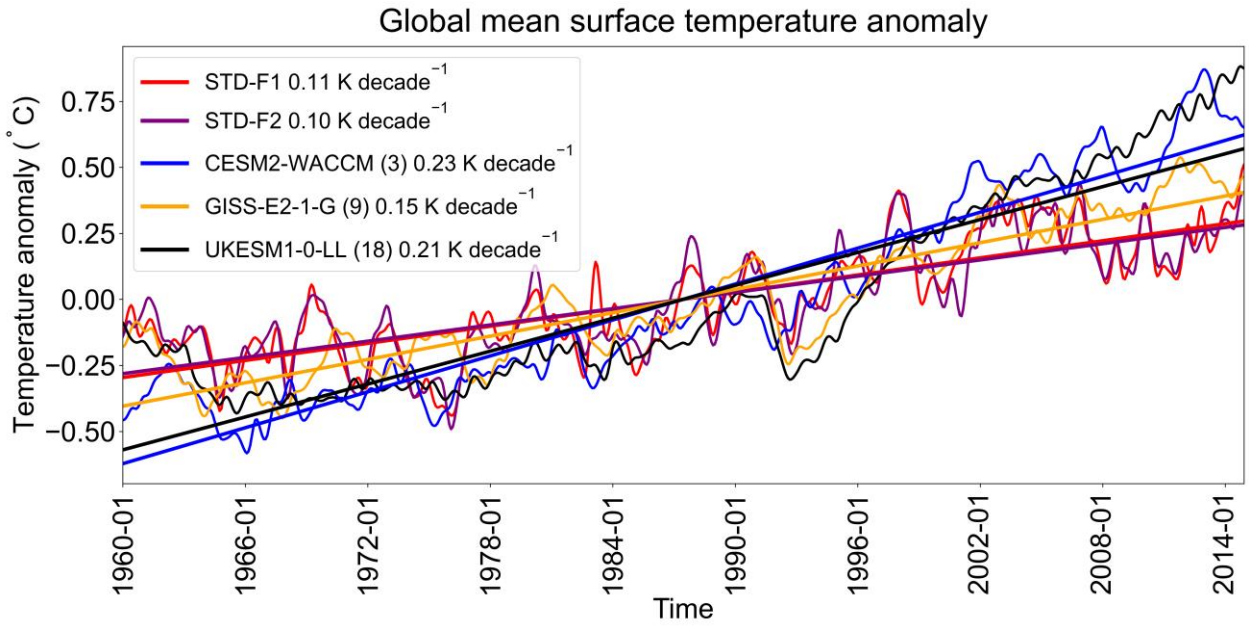

Figure S7: Simulated global mean surface temperature anomalies of our study (CHASER) compared with other CMIP6 models. This figure was created based on the monthly time-series data of global mean surface temperature anomalies with a 1-D Gaussian (Denoising) filter applied. For CMIP6 models, the ensemble mean is shown by the solid line. The fitting curves and the trends of fitting curves (K decade^{-1}) are also presented in this figure.

Table S1: All ensemble members (displayed as variant labels) used for this study.

CESM2-WACCM (3 ensembles)	GISS-E2-1-G (9 ensembles)	UKESM1-0-LL (18 ensembles)
r1i1p1f1	r1i1p3f1	r1i1p1f2
r2i1p1f1	r1i1p5f1	r2i1p1f2
r3i1p1f1	r2i1p5f1	r3i1p1f2
	r3i1p3f1	r4i1p1f2
	r3i1p5f1	r5i1p1f3
	r4i1p3f1	r6i1p1f3
	r4i1p5f1	r7i1p1f3
	r10i1p3f1	r8i1p1f2
	r10i1p5f1	r9i1p1f2
		r10i1p1f2
		r11i1p1f2
		r12i1p1f2
		r14i1p1f2
		r15i1p1f2
		r16i1p1f2
		r17i1p1f2
		r18i1p1f2
		r19i1p1f2